

# Technical note: Rapid and high-resolution deep learning–based radiopharmaceutical imaging with 3D-CZT Compton camera and sparse projection data

Zhiyang Yao<sup>1,2</sup> | Changrong Shi<sup>1,2</sup> | Feng Tian<sup>3</sup> | Yongshun Xiao<sup>1,2</sup> |  
Changran Geng<sup>3</sup> | Xiaobin Tang<sup>3</sup>

<sup>1</sup>Department of Engineering Physics,  
Tsinghua University, Beijing, China

<sup>2</sup>Key Laboratory of Particle & Radiation  
Imaging (Tsinghua University), Ministry of  
Education, Beijing, China

<sup>3</sup>Department of Nuclear Science and  
Technology, Nanjing University of Aeronautics  
and Astronautics, Nanjing, China

## Correspondence

Yongshun Xiao, Department of Engineering  
Physics, Tsinghua University, Beijing 100084,  
China.

Email: xiaoysh@mail.tsinghua.edu.cn

## Funding information

Beijing Municipal Nature Science Foundation,  
Grant/Award Number: 7191005

## Abstract

**Background:** The Compton camera (CC) has great potential in nuclear medicine imaging due to the high detection efficiency and the ability to simultaneously detect multi-energy radioactive sources. However, the finite resolution of the detectors will degrade the images that the real-world CC can obtain. Besides, the CC sometimes can be limited by the detection efficiency, leading to difficulty in using sparse projection data to realize high-resolution reconstruction with short-time measurement, which limits its clinical application for real-time or rapid radiopharmaceutical imaging.

**Purpose:** To overcome the difficulty and promote the usage of the CC in radiopharmaceutical imaging, we present a deep learning (DL)–based CC reconstruction method to realize rapid and high-resolution imaging with short-time measurement.

**Methods:** We developed a DL–based algorithm MCBP-CCnet via Monte Carlo sampling–based back projection and a dedicated convolutional neural network, called CC-Net, to realize the rapid and high-resolution reconstruction with sparse projection data. A CC prototype based on a single three-dimensional position-sensitive CdZnTe (3D-CZT) detector was used to demonstrate the feasibility of our proposed method. The simulations and experiments of radiopharmaceutical imaging used the 3D-CZT CC and [<sup>18</sup>F]NaF. A 3D-printing mouse phantom was also further used to evaluate the performance of the proposed method in animal molecular imaging.

**Results:** The simulation and experimental results showed that the proposed method could realize the images reconstruction within 5 s for list-mode projection data and realized a rapid reconstruction within 35 s for experimental radiopharmaceutical imaging based on the 3D-printing mouse phantom, as well as realized the high-resolution imaging with an accuracy of within 0.78 mm in terms of the sparse projection data that only contained hundreds of events. Besides, the deviations between the reconstructed radiative activities and the exact values were less than 1.51%.

**Conclusion:** The results demonstrated that the proposed method could realize the rapid and high-resolution CC reconstruction with sparse projection data obtained by the 3D-CZT CC and realize the high-resolution radiopharmaceutical imaging. The study in this paper also demonstrated the potential and feasibility of future applications of a 3D-CZT CC for real-time high-resolution radiopharmaceutical imaging with short-time measurement.

**KEYWORDS**

3D-CZT, Compton camera, deep learning, nuclear medical imaging, radiopharmaceutical imaging

**1 | INTRODUCTION**

Radiopharmaceutical imaging gets medical images with the in vivo drugs labeled with specific nuclides. It can provide an accurate diagnosis, enhanced visualization, and more effective personalized treatment for a range of diseases by obtaining the distribution of radiopharmaceuticals in the regions of interest.<sup>1</sup> Currently, existing medical imaging techniques, single-photon emission-computed tomography (SPECT), and positron emission tomography (PET) have played an important role in radiopharmaceutical imaging.<sup>2</sup> However, the energy ranges of gamma rays that they can detect are limited to 511 keV (PET) or other monoenergetic photons (SPECT).<sup>3</sup> The Compton camera (CC) based on electronic collimation, which has the advantages of detecting wide energy ranges of gamma-rays and simultaneously imaging multiple radioactive sources, can overcome the shortcomings of the former and be used in medical imaging.<sup>4</sup>

In recent years, the optimization of designs and reconstruction algorithms of CCs have been investigated by many groups.<sup>5–21</sup> Two main categories of CC are developed with different structures (i.e., single-layer CC and multilayered CC).<sup>7–9</sup> Lots of clinical medical imaging experiments have been carried out with the multilayered CC.<sup>10–12</sup> Multilayered CC utilizes the gamma events interacting with different stages of detectors to obtain the inverted spatial Compton cones that have longer Compton levers (i.e., the distance between the scattering positions and the absorbed positions). The longer Compton levers of multilayered CCs can reduce the effect on the reconstruction accuracy caused by the intrinsic spatial resolution of the detectors. Besides, the events of incomplete energetic deposition can be corrected and used in the reconstruction. However, the multilayered CCs usually are bulkier and more expensive, and most of their reconstruction quality is limited by the inherent energy resolution and spatial resolution due to the scintillation crystals without deep interaction information.<sup>13–15</sup> In contrast, three-dimensional position-sensitive CdZnTe (3D-CZT) semiconductor CC with a compact structure, which has the advantages of a larger field of view, high energy resolution, and spatial resolution, has been developed in recent years.<sup>16,17</sup> Although the shorter Compton levers have a larger effect on the imaging deviation caused by the measurement errors of the spatial interaction positions and the energies deposited, the 3D-CZT CC with portability and large field of view has unique advantages in nuclear medicine imaging.

The high-resolution reconstruction algorithms of CCs for nuclear medicine imaging mainly contain the list-mode maximum likelihood expectation maximization with point spread function (LM-MLEM-PSF) and the origin ensemble with resolution recovery (OE-RR).<sup>18–22</sup> Several groups have demonstrated their performance in nuclear medicine imaging through simulations and experiments. However, the quality of their reconstructed images in clinical experiments was limited by the accuracy of the measured projection data via actual detectors and effective event statistics. For the radiopharmaceutical imaging with a 3D-CZT CC, the existing reconstruction algorithms cannot achieve rapid and high-resolution reconstruction in the case of sparse projection data due to the low detection efficiency and short measurement time.

In the past decade, deep learning (DL) has been widely used in the fields, such as classification, denoising, and segmentation.<sup>23–25</sup> Some recent studies have shown that for CC imaging, DL can generate images close to the truth distribution from low-statistics images, providing new methods for the fast reconstruction of CCs.<sup>26</sup> Besides, DL can give a better estimate of the projection data used for classical algorithms to make a better reconstruction.<sup>27</sup> Inspired by these exciting works, we present a novel DL-based CC algorithm via Monte Carlo sampling-based back projection, and a dedicated neural network designed for CC reconstruction called CC-Net, to promote the nuclear medicine application of 3D-CZT CCs and realize the rapid high-resolution CC reconstruction with sparse projection data. In this paper, we first propose the CC reconstruction algorithm via Monte Carlo sampling-based back projection and CC-Net. Then we introduce the single 3D-CZT CC and 3D-printing mouse phantom, as well as the simulations and experiments scenes. Finally, we evaluate the performance of the proposed method and demonstrate the potential and feasibility of future applications of a 3D-CZT CC for real-time high-resolution radiopharmaceutical imaging with the proposed method.

**2 | MATERIALS AND METHODS****2.1 | Monte Carlo sampling-based back projection and CC-Net**

A Monte Carlo sampling-based back projection (MCBP) proposed in the previous study was used for the pre-processing of the sparse projection data.<sup>28</sup> The MCBP transformed the Compton inverted cones into standard quadratic equations, transformed the algebraic

calculation of the 3D points on the conical surface to two-dimensional random number sampling, and finally realized the 3D fast back projection only by twice independent random sampling. In this study, the resolution recovery process was further optimized and incorporated into the inverted conical calculation based on the Monte Carlo method. That is, the two interaction positions were randomly corrected with independent uniform distributions, and the energies deposited were randomly corrected with two independent Gaussian distributions. The process of corrected MCBP was given by

$$f_{MCBP} = \sum_k \left\{ \delta(v_j, e_i) \mid v_j \in C_i, i \in N \right\} \quad (1)$$

where the  $k$  was the sampling times, the  $v_j$  was the  $j$ th voxel in the field of views in the reconstruction, and the  $e_i$  was the  $i$ th event with total number  $N$ . Its corresponding inversed Compton cones  $C_i$  with resolution recovery could be obtained by

$$C_i = \left\{ (x, y, z) \mid \lambda_1 x_c^2 + \lambda_2 y_c^2 + \lambda_3 z_c^2 = 0, \lambda_i \in f_i(L'_1, L'_2, E'_1, E'_2) \right\} \\ , i = 1, 2 \text{ or } 3 \quad (2)$$

where the  $L'_1$  and  $L'_2$  were the corrected two interaction locations based on the uniform distribution determined by the measured values and the spatial resolution of detectors, and the  $E'_1$  and  $E'_2$  were the corrected two energies deposited based on the Gaussian distribution determined by the measured values and the energy resolution of detectors and the Doppler broadening effect.

Inspired by U-Net for segmentation,<sup>25</sup> we proposed a CC-Net for rapid CC reconstruction with resolution recovery based on the pre-back projection of (1). The architecture of CC-Net is shown in Figure 1. The CC-Net took the reconstructed image with the size  $128 \times 128$  obtained by MCBP as input and generated the denoised and recovered image matrix with the same size as output. To better train the CC-Net, we normalized all the inputs and labels. The CC-Net consisted of the input convolution layers, a down-sampling encoder, an up-sampling decoder, and the output convolution layer. The hyperparameters in the proposed CC-Net are given in Table 1.

## 2.2 | Compton camera and mouse phantom

In this study, we used a 3D-CZT CC produced by Kromek, which was composed of a common planar cathode and  $11 \times 11$  pixelated anode pads and a CZT crystal with the size of  $22 \times 22 \times 15 \text{ mm}^3$ . The 3D coordinates of Compton events could be obtained from the horizontal spatial location of pixelating anode pads

and the depth calculated by the time difference between the signals of the cathode and the anode.<sup>29</sup> The spatial resolution of the 3D-CZT CC was 1 mm for the lateral position as well as the depth, and the energy resolution at 511 keV was about 1.5% (Figure 2).

The cryosection images of a 28-g nude male mouse and coregistered CT were used to generate a mouse phantom.<sup>2,3</sup> As shown in Figure 2, the Butanediol dimethacrylate ( $C_{12}H_{18}O_4$ ,  $\rho$ :  $1.3 \text{ g/cm}^3$ )-based 3D-printing mouse phantom contained five areas to place the radiopharmaceutical (i.e., brain, heart, two kidneys, and bladder).

## 2.3 | Simulations

The simulation was based on the Geant4.p.10.03. The simulated CC referred to the built 3D-CZT CC and was modeled with the same spatial and energy resolution and the same size. Two simulations were implemented to train the CC-Net together. The field of view in the reconstructions was the squares with a side length of 10 cm. In addition, their two-dimensional pixelate array was  $128 \times 128$ .

### 2.3.1 | Radiopharmaceuticals were randomly and irregularly distributed in organs

The radiopharmaceutical,  $[^{18}\text{F}]\text{NaF}$ , was assumed to be randomly injected into the brain, heart, kidney, and bladder at different doses. Thus, the radiative sources with the energy at 511 keV and different distributions in these five characteristic areas were randomly generated in each simulation. We also stored their exact spatial distributions of sources as labels in training and used the primary reconstructions based on MCBP as the inputs for the CC-Net. In particular, the simulated radiation source distribution in these five different parts was completely random, with different geometry and intensity, which was not limited by the shape of the five organs; so it covered all possible radiation source distribution characteristics in practical situations. The simulations were implemented 24000 times. A total of 19200 groups were used as training sets, and the other 4800 groups were used as testing sets.

### 2.3.2 | Radiopharmaceuticals were randomly and irregularly distributed in organs and with metastasis

Gaussian-broadened diffused point-like sources with different numbers were additionally randomly distributed in the field of view in simulations based on the 3D-printing mouse phantom earlier. The maximum number of sources was five, and the numbers of sources were

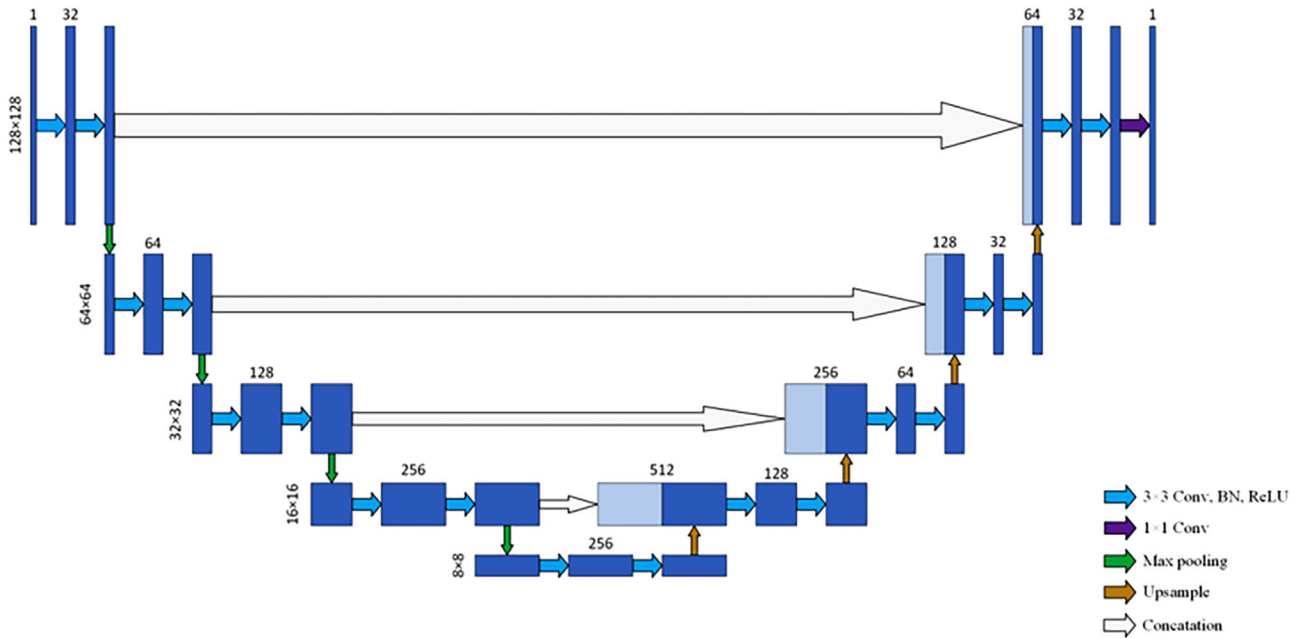


FIGURE 1 The architecture of CC-Net

TABLE 1 The hyperparameters of the proposed CC-Net

Patch size	128 × 128
Convolution layer filter size	3 × 3
Up-sampling layer filter size	2 × 2
Learning rate range	[1e <sup>-4</sup> , 1e <sup>-5</sup> ]
Size of mini-batch	4

randomly chosen. Besides, the standard errors of their Gaussian distribution were randomly obtained from 0.7 to 4.2 mm, and the emitted gamma-rays from the sources were 511 keV. The mixed sources were used to simulate the possible metastasis of radiopharma-

ceuticals in the mouse phantom. The simulations were implemented 12000 times. A total of 9600 groups were used as training sets, and the other 2400 groups were used as testing sets.

The interaction positions in the list-mode projection data obtained in simulations were moved to the pixel center of the detector unit, and the deposited energies were randomly corrected with a Gaussian distribution determined by the energy resolution of the CC. Besides, the information of projection data was randomly inverted (i.e., exchanged the information of the scattering point with that of the absorption point in the list-mode data), to simulate the projection data obtained from the real-world 3D-CZT CC. All the training images were randomly rotated or flipped before being inputted into the CC-Net.

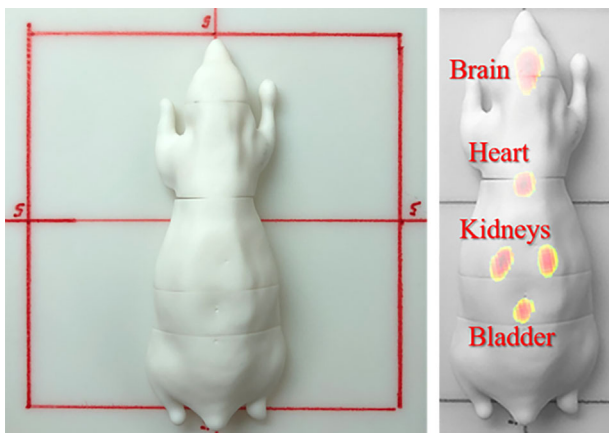


FIGURE 2 The photograph and schematic diagram of the internal structure of the three-dimensional (3D)-printing mouse phantom

## 2.4 | Experiments

In the experiments, [<sup>18</sup>F]NaF solution, provided by JYAMS PET Research and Development Limited, was placed in a sealed capsule that was located in the brain and kidneys, and bladder with ~14 and ~7 and ~7 μCi, respectively. The phantom was placed about 10 cm above the detector, and the center of the CZT crystal was basically aligned with the phantom. The experiments detected the presence of radiopharmaceuticals in the brain and kidneys and bladder separately or at the same time. Each group of experiments was measured for 1 h, and the detection data were output every 15 min.

All these list-mode projection data were randomly divided into independent event sets according to the equivalent photon events detected in 30 s. Then all the

experimental datasets were reconstructed by the MCBP and imported into the trained CC-Net via the simulations to obtain the reconstruction results directly.

## 2.5 | Training strategies

The mean square error (MSE) was used as the loss function for training CC-Net:

$$L = MSE = \frac{1}{M \times K} \|f - \hat{f}\|_2^2 \quad (3)$$

where the  $\hat{f}$  was the predicted image, and the  $f$  was the corresponding label. The  $M$  and  $K$  were the number of row and column pixels, respectively. An Adam optimizer<sup>30</sup> was used for training with  $\beta_1 = 0.9$ ,  $\beta_2 = 0.999$ , and  $\epsilon = 10^{-8}$ . The batch size was 4, and we trained 30 epochs in total. The learning rate was set to  $10^{-4}$  and decayed to  $10^{-5}$  in 20 epochs.

The training was performed on PyTorch framework with Python language.<sup>31</sup> In addition, the training took  $\sim 4$  h on one NVIDIA TITAN RTX GPU card.

## 2.6 | Evaluation method

Three metrics were used to evaluate the reconstructed image quality and compared with the exact values in this study. They were MSE that is given by Equation (3), peak signal-to-noise ratio (PSNR), and structural similarity index metric (SSIM):

$$PSNR = 10 \log_{10} \frac{\max(f, \hat{f})}{MSE} \quad (4)$$

$$SSIM = \frac{(2\mu_{\hat{f}}\mu_f + c_1)(2\sigma_{\hat{f},f} + c_2)}{(\mu_{\hat{f}}^2 + \mu_f^2 + c_1)(\sigma_{\hat{f}}^2 + \sigma_f^2 + c_2)} \quad (5)$$

where the  $\max(f, \hat{f})$  denoted the maximum possible pixel value, which was 1 in all experiments.  $\mu_{\hat{f}}$  and  $\mu_f$  were the mean value of  $\hat{f}$  and  $f$ .  $\sigma_{\hat{f}}$  and  $\sigma_f$  were the variance of  $\hat{f}$  and  $f$ .  $\sigma_{\hat{f},f}$  was the covariance of  $\hat{f}$  and  $f$ , and constant  $c_1 = 0.01^2$ ,  $c_2 = 0.03^2$ .

In addition, two iterative CC reconstruction algorithms were used to compare with the proposed DL-based algorithm. One was the LM-MLEM-PSF algorithm, a kind of LM-MLEM algorithm with the pre-estimated PSF to recover the resolutions<sup>18</sup> (abbreviated as MLEM-PSF as follows). The other one was the subset-driven OE-RR (SD-OE-RR) algorithm, a recently proposed OE-RR algorithm with a faster iterative speed<sup>29</sup> (abbreviated as OE-RR as follows).

## 3 | RESULTS

### 3.1 | Radiopharmaceutical imaging based on simulated 3D-printing mouse phantom

As shown in Figure 3, when the projection data was sparse (i.e., only hundreds of effective events), due to the spatial resolution of the detectors and the low statistics, the results obtained by the MCBP could not obtain the roughly accurate distributions of the radiopharmaceuticals especially for the sources with a short distance. Although the iterative reconstruction algorithms with resolution recovery could restore the degraded reconstructed image to a certain extent, the sparse projection data and the lack of sufficient statistical properties could cause the loss of lower activity radioactive sources or the deviations in the reconstruction. The proposed method could recover the degraded images and reproduce the exact radiopharmaceutical distribution, even if there were randomly existed in the phantom without any regular distribution. As Figure 4 shown, the profiles obtained by the proposed method were almost identical to the exact corresponding profiles of the value, and the accuracy was within 0.5 mm. In each group of reconstruction results in Figure 4, two contours with as many features as possible at the position of the red dotted line are selected to evaluate the reconstruction accuracy of the proposed method. Besides, the profiles containing less obvious but important features, such as the radiative distribution in the heart of the mouse phantom in Group 3 in Figure 3, were also selected. As shown in Table 2, the proposed method could obtain better reconstruction images compared to the reconstructions obtained by the MCBP and LM-MLEM-PSF and SD-OE-RR.

### 3.2 | Radiopharmaceutical imaging simulations with random metastasis

As shown in Figures 5 and 6, for the more complex distributions of the radiopharmaceuticals, the proposed method could reconstruct most of the exact distributions, although the MCBP-based reconstruction results for input to CC-Net have been severely distorted due to sparse projection data (about 400 events). In contrast, the LM-MLEM-PSF and SD-OE-RR algorithms could not reconstruct the complex distributions due to the lack of enough source information obtained from the sparse and nonideal projection data. As shown in Table 3, the proposed method could obtain better reconstructions with lower MSEs, higher PSNRs, and higher SSIMs compared with that of the MCBP and two iterative algorithms (Table 4).

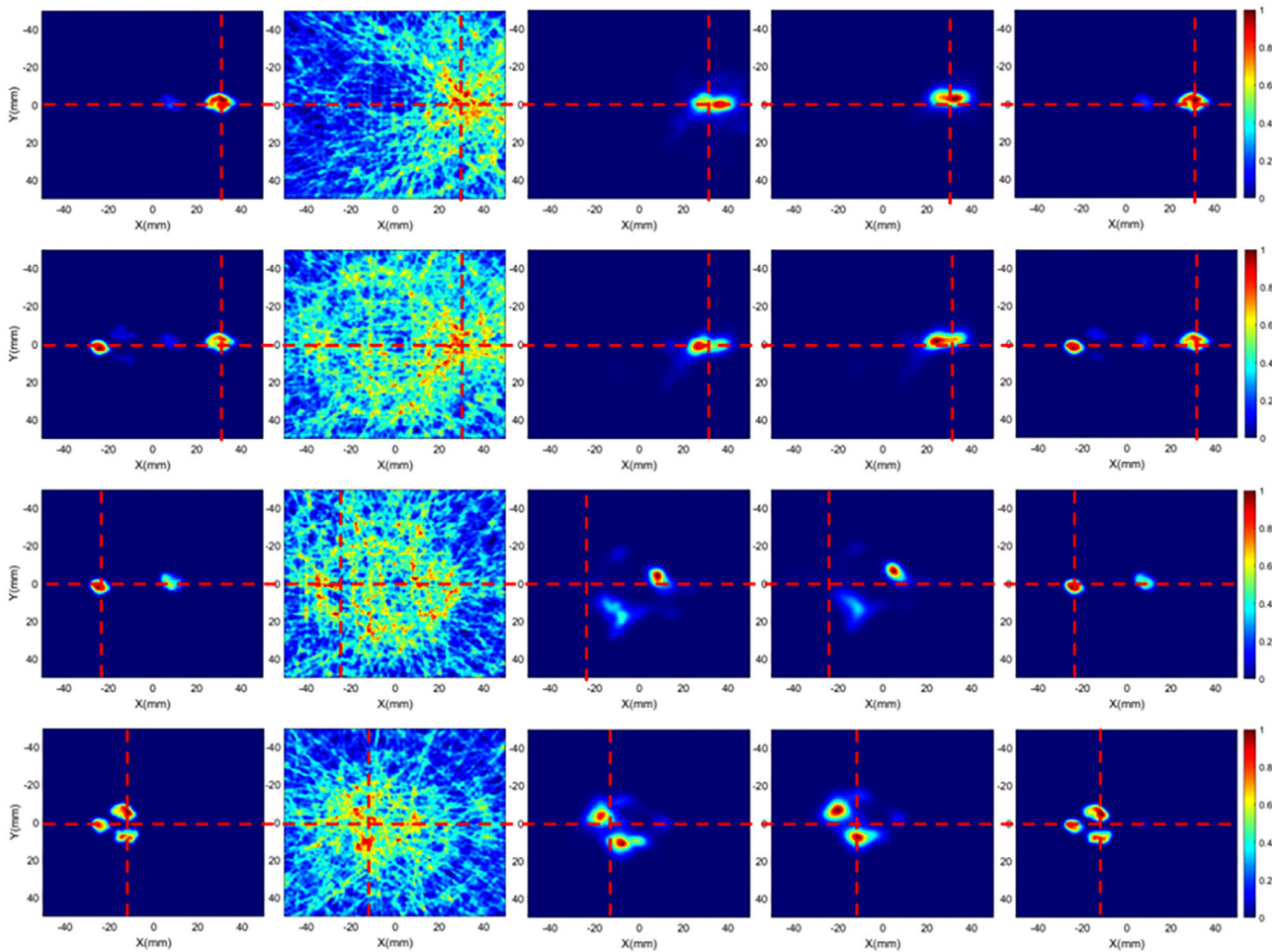


**FIGURE 3** The two-dimensional (2D) projection results of part of simulations of radiopharmaceutical imaging based on 3D-printing mouse phantom, where the radiopharmaceuticals were distributed randomly and irregularly in organs. The columns from the left to right were the exact distributions of radiopharmaceuticals and the reconstruction results of the Monte Carlo back projection (MCBP), list-mode maximum likelihood expectation maximization with point spread function (LM-MLEM-PSF), subset-driven origin ensemble with resolution recovery (SD-OE-RR), and the proposed MCBP-CCnet, respectively. The red dotted line in the figures represents the profiles selected in Figure 4.

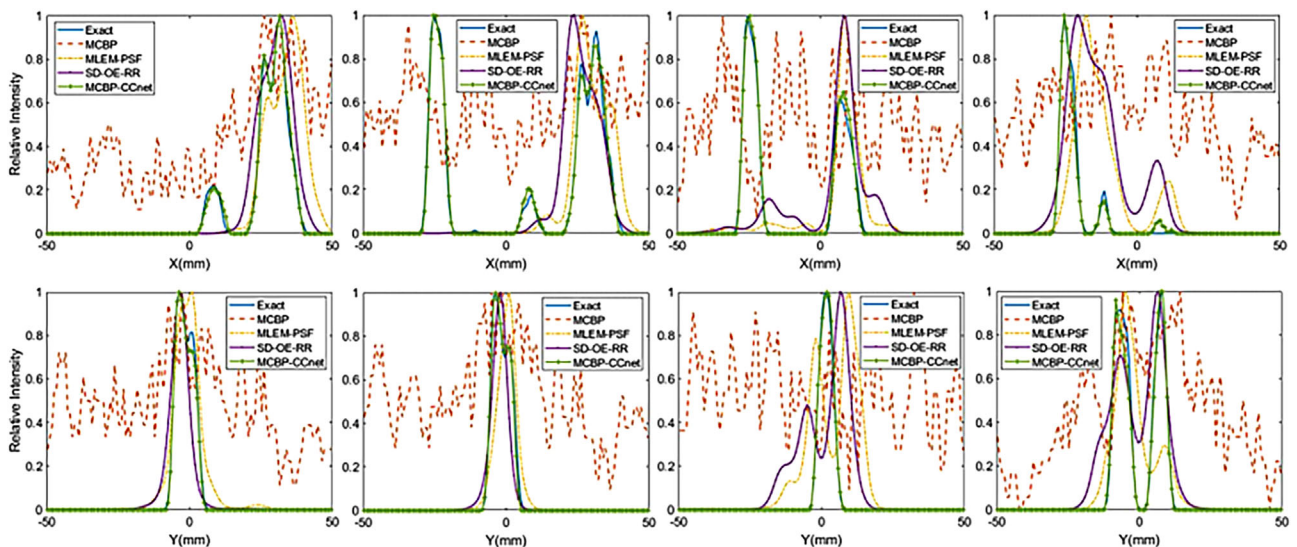


**FIGURE 4** The comparison of the profiles in part of simulations of radiopharmaceutical imaging based on three-dimensional (3D)-printing mouse phantom

**TABLE 2** The results of different methods for the four simulation datasets shown in Figure 3

Methods	Simulation S#1			Simulation S#2			Simulation S#3			Simulation S#4		
	MSE	PSNR	SSIM									
MCBP	0.1449	8.3897	0.0056	0.2286	6.4086	0.0059	0.1639	7.8536	0.0039	0.1160	9.3553	0.0056
MLEM-PSF	0.0500	13.0105	0.8792	0.0848	10.7148	0.8663	0.0442	13.5446	0.8601	0.0262	15.8252	0.8781
OE-RR	0.0481	13.7918	0.9231	0.0838	10.7686	0.8737	0.0476	13.2371	0.8794	0.0257	15.8969	0.8890
MCBP-CCnet	<b>0.0001</b>	<b>47.0742</b>	<b>0.9970</b>	<b>0.0001</b>	<b>48.6673</b>	<b>0.9996</b>	<b>0.0001</b>	<b>50.2081</b>	<b>0.9997</b>	<b>0.0001</b>	<b>42.7758</b>	<b>0.9979</b>

Note: The simulation S#1, S#2, S#3, and S#4 represented the four sets from the top to the bottom, respectively.

Abbreviations: MCBP, Monte Carlo back projection; MLEM-PSF, maximum likelihood expectation maximization with point spread function; MSE, mean square error; OE-RR, origin ensemble with resolution recovery; PSNR, peak signal-to-noise ratio; SSIM, similarity index metric.

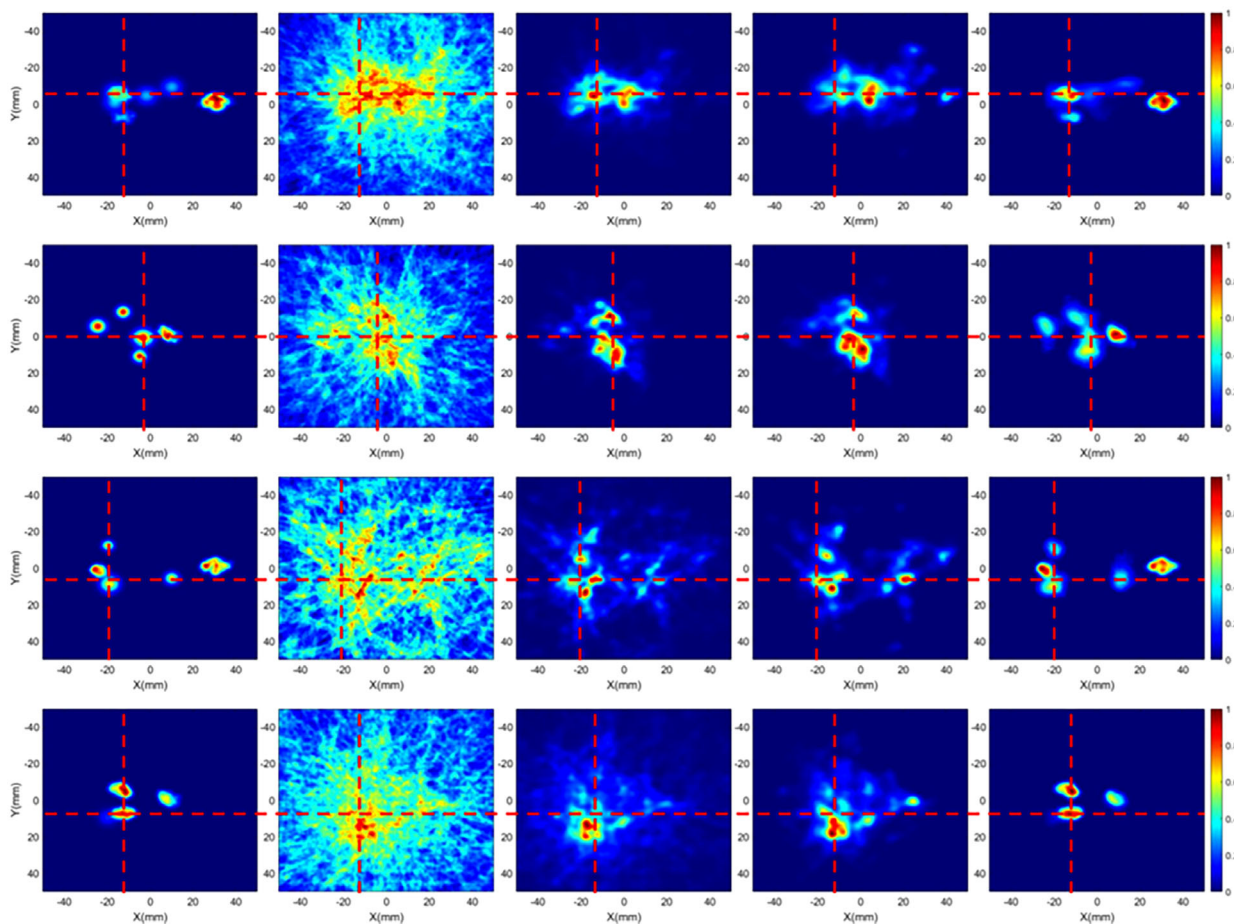


**FIGURE 5** The 2D projection results of part of simulations of radiopharmaceutical imaging based on three-dimensional (3D)-printing mouse phantom, where the radiopharmaceuticals were distributed randomly and irregularly in organs as well as with random metastasis. The columns from the left to right were the exact distributions of radiopharmaceuticals, the reconstruction results of the Monte Carlo back projection (MCBP), list-mode maximum likelihood expectation maximization with point spread function (LM-MLEM-PSF), subset-driven origin ensemble with resolution recovery (SD-OE-RR), and the proposed MCBP-CCnet, respectively. The red dotted line in the figures represents the profiles selected in Figure 6.

### 3.3 | Radiopharmaceutical imaging experiments

As shown in Figure 7, for the experiments, with the projection data less than 3000 effective events with a measurement time of 30 s, the results obtained by the MCBP could roughly distinguish the radioactive

sources in different regions. The results obtained by the LM-MLEM-PSF and the SD-OE-RR were better when the sources were distributed in a single tissue area, such as the bladder, whereas there would be severe distortion for radioactive sources distributed over multiple or greater tissue areas (e.g., existing simultaneously in the head and bladder, or two kidneys). In contrast,

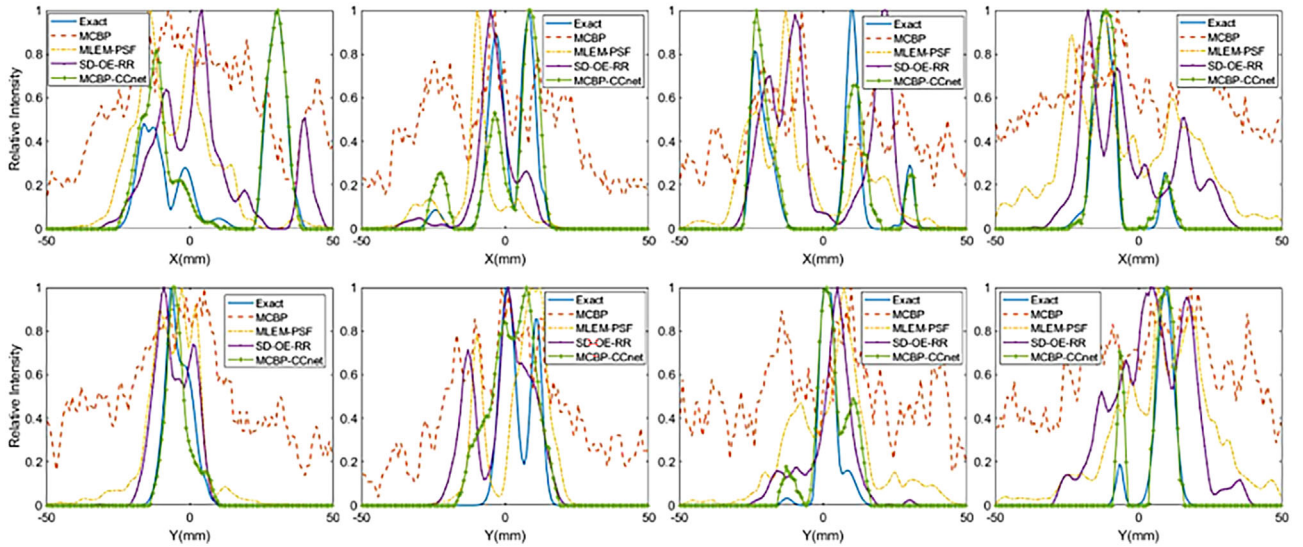


**FIGURE 6** The comparison of the profiles in part of simulations of Figure 5 based on three-dimensional (3D)-printing mouse phantom

**TABLE 3** The results of different methods for the four simulation datasets shown in Figure 5

Methods	Simulation M#1			Simulation M#2			Simulation M#3			Simulation M#4		
	MSE	PSNR	SSIM									
MCBP	0.1257	9.0060	0.0105	0.0832	10.7968	0.0171	0.1292	8.8883	0.0026	0.1451	8.3847	0.0074
MLEM-PSF	0.0106	19.7447	0.7460	0.0109	19.6422	0.8044	0.0123	19.0895	0.4678	0.0150	18.2320	0.2885
OE-RR	0.0116	25.3596	0.7776	0.0100	26.0158	0.8447	0.0120	25.5303	0.7321	0.0117	25.3413	0.7272
MCBP-CCnet	<b>0.0006</b>	<b>32.1072</b>	<b>0.9646</b>	<b>0.0028</b>	<b>25.4875</b>	<b>0.9234</b>	<b>0.0011</b>	<b>29.7393</b>	<b>0.9515</b>	<b>0.0001</b>	<b>41.7698</b>	<b>0.9957</b>

Note: The simulations M#1, M#2, M#3, and M#4 represented the four sets from the top to the bottom, respectively.

Abbreviations: MCBP, Monte Carlo back projection; MLEM-PSF, maximum likelihood expectation maximization with point spread function; MSE, mean square error; OE-RR, origin ensemble with resolution recovery; PSNR, peak signal-to-noise ratio; SSIM, similarity index metric.

**TABLE 4** The results of different methods for the four experimental datasets

Methods	Experiment 1			Experiment 2			Experiment 3			Experiment 4		
	MSE	PSNR	SSIM									
MCBP	0.0375	5.1222	0.0246	0.1872	7.2780	0.0054	0.1690	7.7213	0.03221	0.1917	7.1746	0.0359
MLEM-PSF	0.0318	14.9825	0.5113	0.0076	21.2114	0.8253	0.0006	32.1268	0.8009	0.0046	23.4194	0.8229
OE-RR	0.0212	16.7312	0.5948	0.0071	21.4649	0.8320	0.0010	29.9797	0.8005	0.0010	29.8964	0.8431
MCBP-CCnet	<b>0.0001</b>	<b>40.9686</b>	<b>0.8606</b>	<b>0.0001</b>	<b>39.0269</b>	<b>0.7850</b>	<b>0.0001</b>	<b>39.9367</b>	<b>0.8156</b>	<b>0.0002</b>	<b>37.7713</b>	<b>0.8545</b>

Note: The #1, #2, #3, and #4 represented a randomly selected testing dataset from head and bladder, kidneys, bladder, and head in Figure 7, respectively.

Abbreviations: MCBP, Monte Carlo back projection; MLEM-PSF, maximum likelihood expectation maximization with point spread function; MSE, mean square error; OE-RR, origin ensemble with resolution recovery; PSNR, peak signal-to-noise ratio; SSIM, similarity index metric.

the output images processed by CC-Net were almost completely consistent with the accurate distribution in the spatial distribution and the relative intensity of the radioactive sources. The time consumption for obtaining the final reconstruction images was also less than 5 s. As shown in Table 4, the reconstructions obtained by the proposed method could have better image quality compared to the reconstructions obtained by the MCBP, LM-MLEM-PSF, and SD-OE-RR algorithms in terms of the MSE, PSNR, and SSIM, respectively (Figure 8).

### 3.4 | Overall performance of the MCBP-CCnet

The decreasing trend of loss was almost the same and the loss was almost equal after reaching the preset epochs, which showed that the trained model had almost no overfitting. As shown in Table 5, the results based on the trained model had close metrics on the simulated test set and all experimental datasets, demonstrating the robustness of the proposed method.

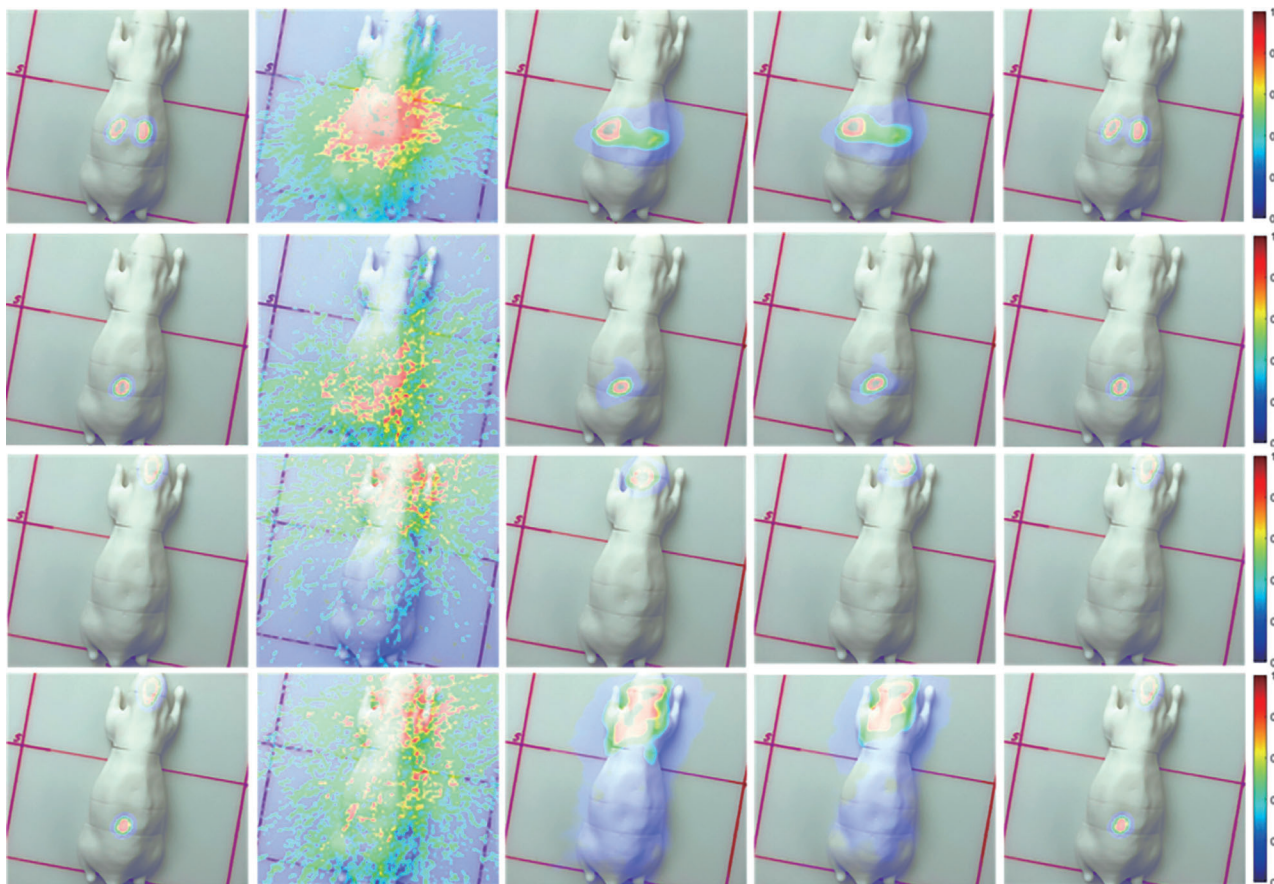


**FIGURE 7** The 2D projection results of part of experiments of radiopharmaceutical imaging based on three-dimensional (3D)-printing mouse phantom. The columns from the left to right were the exact distributions of radiopharmaceuticals, the reconstruction results of the Monte Carlo back projection (MCBP), list-mode maximum likelihood expectation maximization with point spread function (LM-MLEM-PSF), subset-driven origin ensemble with resolution recovery (SD-OE-RR), and the proposed MCBP-CCnet, respectively. All the distributions of the radiative sources were of registration with the actual 3D-printing mouse phantom.

**TABLE 5** The overall performance of the MCBP-CCnet in the three different testing datasets

Testing datasets	MSE	PSNR	SSIM
Radiopharmaceuticals simulation (irregularly and randomly distributed in organs)	0.0001	41.8937	0.9120
Radiopharmaceuticals simulations with metastasis (irregularly and randomly distributed in organs)	0.0004	36.1935	0.9709
Radiopharmaceutical experiments based on a 3D-printing mouse phantom	0.0004	38.1301	0.8333

Abbreviations: 3D, three-dimensional; MSE, mean square error; PSNR, peak signal-to-noise ratio; SSIM, similarity index metric.

## 4 | DISCUSSION

In this study, we took the advantage of the MCBP to obtain fast pre-back projection images while achieving the resolution recovery and then used the CC-Net to obtain the accurate reconstruction results by using

the characteristics of the preliminary reconstructed distribution. The computational complexity of our further modified MCBP was  $O(N \times k)$ , where  $k$  was the product of the number of random sampling per event and the number of resolution corrections per projection data. For 3000 events, the reconstruction took about 4 s. The proposed CC-Net could achieve resolution recovery and image enhancement through feature extraction. For the inputs with the  $128 \times 128$  matrix in the reconstruction where the side length of the pixels in the field of views was 0.78 mm, the prediction time was less than 0.009 s.

As shown in Figure 3, the trained CC-Net with MCBP could be applied to the reconstructions of all random and irregular radiopharmaceutical distribution with an accuracy of within 0.78 mm for the maximum intensity positions. Although the absolute intensities were slightly different, the relative intensity deviations of the overall radiation source were less than 0.0001 in terms of MSE. Besides, for the cross-sectional view passing through the radioactive sources within the region of interest in Figure 4, the deviations of the complex edges were less than 1 mm, demonstrating the feasibility of the proposed

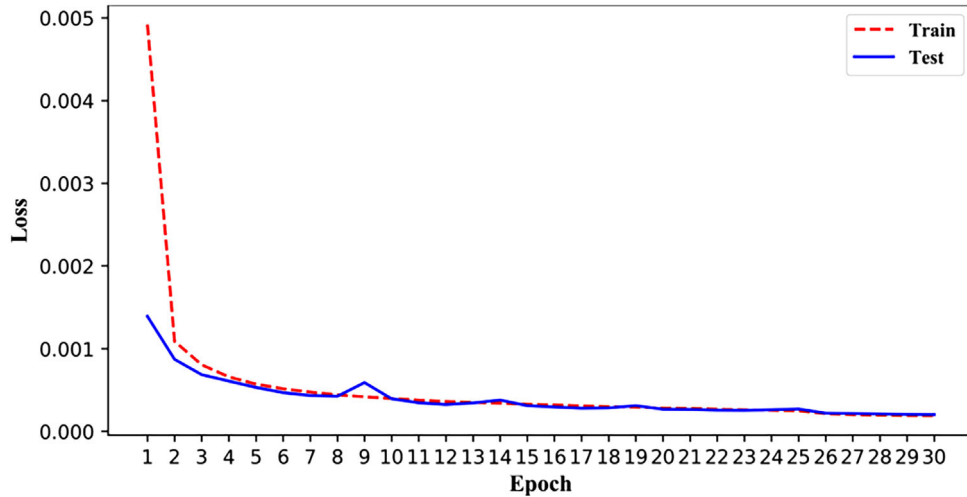


**FIGURE 8** The comparison of the loss (i.e., the mean square error [MSE] between the prediction obtained by the MCBP-CCnet and the label [exact values]) for the training sets and testing sets.

method for resolution recovery and high-resolution CC reconstruction.

For the radiopharmaceutical imaging based on a simulated 3D-printing mouse phantom with the irregular distribution in organs and random metastasis, the proposed method successfully realized the reconstruction of the complex radiopharmaceutical distributions in the phantom with sparse projection data. The MSE metric was about 0.0004, which was promising to realize an accurate reconstruction of the irregular distribution in different organs and the in vivo possible metastasis of the radiopharmaceutical. As the coincidence events obtained during actual measurement could have very short Compton levers, such as less than 2 mm, which was close to the positional deviation of depth measurement, the spatial deviation of the Compton cone was larger due to the deviation of projection data. Moreover, the lack of sufficient temporal resolution in the experiment further increased the bias of the reconstruction by incorrectly deciding whether the action position was a scattering point or an absorbed point. Thus, the preliminary reconstruction obtained by MCBP had a larger level of positional deviations and background noise. In this case, the proposed method trained by the simulated data was implemented successfully in the experimental data, although the metrics for the experimental datasets were lower than the simulation of radiopharmaceuticals distributed irregularly in organs. However, due to the limitation of the shape of the capsule in the 3D-printing mouse phantom and the volume of radiopharmaceuticals that can be accommodated, the exact spatial distributions of the radioactive sources in the experimental data had fewer features compared to the simulated data. Thus, the PNSR metrics for the experimental datasets were higher than the simulation of radiopharmaceuticals distributed irregularly in

organs with random metastasis, the source distributions of which were more complex. There was almost no overfitting in the trained CC-Net because of the close metrics on the simulated training sets and testing sets. In addition, the results demonstrated the feasibility of the experimental high-resolution reconstruction via the proposed method trained in the simulations, where the MSE of all experimental datasets obtained by the proposed method was 0.0004. Moreover, the projection data used in the reconstructions were only obtained by the detection time of 30 s. Although the simulated data closer to the actual measurement or pre-preliminary measurement for calibration was required for the CC-Net training in future clinical applications, the results showed the potential for the future dynamic real-time monitoring of in vivo radiopharmaceuticals with the 3D-CZT CC and the proposed method.

In contrast to existing radiopharmaceutical imaging techniques, our study provides an approach that combined a DL-based reconstruction method and a 3D-CZT CC. On the one hand, we investigated the method of rapid and high-resolution radiopharmaceutical imaging with the 3D-CZT CC and further presented its potential for dynamic monitoring in future nuclear medicine imaging. On the other hand, we propose a DL-based CC reconstruction method, overcoming the difficulty of the current iterative and analytical algorithms in realizing the rapid and high-resolution reconstruction with the sparse projection data.

## 5 | CONCLUSION

In this study, we propose a DL-based CC algorithm via Monte Carlo sampling-based back projection and CC-Net. The simulation and experiment results demonstrated that the method could realize the rapid and

high-resolution CC reconstruction with sparse projection data obtained by the 3D-CZT CC. We realized the rapid reconstruction within 35 s for experimental radiopharmaceutical imaging based on a 3D-printing mouse phantom, and the high-resolution imaging with the accuracy of within 0.78 mm in terms of the sparse projection data, which only contained hundreds of events. The study in this paper also demonstrated the potential and feasibility of future applications of a 3D-CZT CC for real-time high-resolution radiopharmaceutical imaging with short-time measurement.

## ACKNOWLEDGMENT

This work was supported by Beijing Municipal Nature Science Foundation (Grant no. 7191005).

## CONFLICT OF INTEREST

The authors have no relevant conflicts of interest to disclose.

## REFERENCES

- Filippou V, Tsoumpas C. Recent advances on the development of phantoms using 3D printing for imaging with CT, MRI, PET, SPECT, and ultrasound. *Med Phys*. 2018;45:e740-e760
- Del Guerra A, Belcari N. State-of-the-art of PET, SPECT and CT for small animal imaging. *Nucl Instrum Methods Phys Res, Sect A*. 2007;583:119-124
- Sato S, Kataoka J, Kotoku J, et al. High-statistics image generation from sparse radiation images by four types of machine-learning models. *J Instrum*. 2020;15(10):P10026.
- Fontana M, Dauvergne D, Létang JM, Ley J-L, Testa É. Compton camera study for high efficiency SPECT and benchmark with anger system. *Phys Med Biol*. 2017;62:8794
- Kabuki S, Hattori K, Kohara R, et al. Development of electron tracking Compton camera using micro pixel gas chamber for medical imaging. *Nucl Instrum Methods Phys Res, Sect A*. 2007;580:1031-1035
- Roellinghoff F, Richard M-H, Chevallier M, et al. Design of a Compton camera for 3D prompt- $\gamma$  imaging during ion beam therapy. *Nucl Instrum Methods Phys Res, Sect A*. 2011;648:S20-S3
- Watanabe S, Tanaka T, Nakazawa K, et al. A Si/CdTe semiconductor Compton camera. *IEEE Trans Nucl Sci*. 2005;52:2045-2051
- Kataoka J, Kishimoto A, Nishiyama T, et al. Handy Compton camera using 3D position-sensitive scintillators coupled with large-area monolithic MPPC arrays. *Nucl Instrum Methods Phys Res, Sect A*. 2013;732:403-407
- Turecek D, Jakubek J, Trojanova E, Sefc L. Single layer Compton camera based on Timepix3 technology. *J Instrum*. 2020;15:C01014
- Solevi P, Munoz E, Solaz C, et al. Performance of MACACO Compton telescope for ion-beam therapy monitoring: first test with proton beams. *Phys Med Biol*. 2016;61:5149
- Sakai M, Yamaguchi M, Nagao Y, et al. In vivo simultaneous imaging with  $^{99m}\text{Tc}$  and  $^{18}\text{F}$  using a Compton camera. *Phys Med Biol*. 2018;63:205006
- Thirolf P, Aldawood S, Böhmer M, et al. A Compton camera prototype for prompt gamma medical imaging. EPJ Web of Conferences. *Nucl Struct*. 2016;117:05005
- Abbaspour S, Mahmoudian B, Islamian JP. Cadmium telluride semiconductor detector for improved spatial and energy resolution radioisotopic imaging. *World J Nucl Med*. 2017;16:101
- Takeda SI, Odaka H, Ishikawa S-N, et al. Demonstration of in-vivo multi-probe tracker based on a Si/CdTe semiconductor Compton camera. *IEEE Trans Nucl Sci*. 2012;59:70-76
- Suzuki Y, Yamaguchi M, Odaka H, et al. Three-dimensional and multienergy gamma-ray simultaneous imaging by using a Si/CdTe Compton camera. *Radiology*. 2013;267:941-947
- Feng Z, Zhong H, Dan X. Analysis of detector response using 3-D position-sensitive CZT gamma-ray spectrometers. *IEEE Trans Nucl Sci*. 2005;51:3098-3104
- Liu Y-L, Fu J-Q, Li Y-L, Li Y-J, Ma X-M, Zhang L. Preliminary results of a Compton camera based on a single 3D position-sensitive CZT detector. *Nucl Sci Tech*. 2018;29:1-11
- Kim SM, Seo H, Park JH, et al. Resolution recovery reconstruction for a Compton camera. *Phys Med Biol*. 2013;58(9):2823.
- Jan ML, Lee MW, Huang HM. PSF reconstruction for Compton-based prompt gamma imaging. *Phys Med Biol*. 2018;63(3):035015.
- Andreyev A, Celler A, Ozsahin I, Sitek A. Resolution recovery for Compton camera using origin ensemble algorithm. *Med Phys*. 2016;43(8 pt 1):4866-4876.
- Yao Z, Xiao Y, Chen Z, et al. Compton-based prompt gamma imaging using ordered origin ensemble algorithm with resolution recovery in proton therapy. *Sci Rep*. 2019;9(1):1133.
- Yao Z, Yuan Y, Wu J, et al. Rapid Compton camera imaging for source terms investigation in the nuclear decommissioning with a subset-driven origin ensemble algorithm. *Radiat Phys Chem*. 2022;197:110133. <https://doi.org/10.1016/j.radphyschem.2022.110133>
- Krizhevsky A, Sutskever I, Hinton GE. ImageNet classification with deep convolutional neural networks. *Adv Neural Inf Proc Sys*. 2012;25:1097-1105
- Zhang K, Zuo W, Chen Y, Meng D, Zhang L. Beyond a Gaussian Denoiser: residual learning of deep CNN for image denoising. *IEEE Trans Image Process*. 2017;26:3142-3155
- Ronneberger O, Fischer P, Brox T. U-net: convolutional networks for biomedical image segmentation. International Conference on Medical Image Computing and Computer-Assisted Intervention. 2015:234-241
- Daniel G, Gutierrez Y, Limousin O. Application of a deep learning algorithm to Compton imaging of radioactive point sources with a single planar CdTe pixelated detector. *Nucl Eng Technol*. 2022;54:1747-1753.
- Ikeda T, Takada A, Abe M, et al. Development of convolutional neural networks for an electron-tracking Compton camera. *Prog Theor Exp Phys*. 2021;2021(8):083F01.
- Yao Z, Xiao Y, Wang B, et al. Study of 3D fast Compton camera image reconstruction method by algebraic spatial sampling. *Nucl Inst Methods Phys Res, A*. 2018;954:161345. <https://doi.org/10.1016/j.nima.2018.10.023>
- He Z, Li W, Knoll GF, Wehe DK, Berry J, Stahle CM. 3-D position sensitive CdZnTe gamma-ray spectrometers nuclear instruments and methods in physics. *Nucl Instrum Methods Phys Res, Sect A*. 1999;422:173-178
- Kingma DP, Ba J. Adam: a method for stochastic optimization. 2014. arXiv preprint arXiv:1412.6980.
- Paszke A, Gross S, Massa F, et al. PyTorch: an imperative style, high-performance deep learning library. *Adv Neural Inf Proc Sys*. 2019;32:8024-8035.

**How to cite this article:** Yao Z, Shi C, Tian F, Xiao Y, Geng C, Tang X. Technical note: Rapid and high-resolution deep learning-based radiopharmaceutical imaging with 3D-CZT Compton camera and sparse projection data. *Med Phys*. 2022;1-11. <https://doi.org/10.1002/mp.15898>